Volume 1 | Number 1 | Jan 2013 | Pages 1–100

Journal of
Materials Chemistry C

Materials for optical and electronic devices
www.rsc.org/materialsC

ROYAL SOCIETY
OF CHEMISTRY

ROYAL SOCIETY
OF **CHEMISTRY**

www.rsc.org/materialsC

High Temperature Thermoelectric Properties of Zn-doped Eu$_5$In$_2$Sb$_6$

Sevan Chanakian[1], Umut Aydemir[1*], Alex Zevalkink[1,2], Zachary M. Gibbs[3], Jean-Pierre Fleurial[2], Sabah Bux[2], G. Jeffrey Snyder[1]

[1] Department of Applied Physics and Materials Science, California Institute of Technology, 1200 E California Blvd, Pasadena, USA

[2] Thermal Energy Conversion Technologies Group, Jet Propulsion Laboratory, 4800 Oak Grove Drive, Pasadena, USA

[3] Division of Chemistry and Chemical Engineering, California Institute of Technology, 1200 E California Blvd, Pasadena, USA

Abstract

The complex bonding environment of many ternary Zintl phases, which often results in low thermal conductivity, makes them strong contenders as thermoelectric materials. Here, we extend the investigation of A_5In$_2$Sb$_6$ Zintl compounds with the Ca$_5$Ga$_2$As$_6$ crystal structure to the only known rare-earth analogue: Eu$_5$In$_2$Sb$_6$. Zn-doped samples with compositions of Eu$_5$In$_{2-x}$Zn$_x$Sb$_6$ (x = 0, 0.025, 0.05, 0.1, 0.2) were synthesized via ball milling followed by hot pressing. Eu$_5$In$_2$Sb$_6$ showed significant improvements in air stability relative to its alkaline earth metal analogues. Eu$_5$In$_2$Sb$_6$ exhibits semiconducting behavior with possible two band behavior suggested by increasing band mass as a function of Zn content, and two distinct transitions observed in optical absorption measurements (at 0.15 and 0.27 eV). The p-type Hall mobility of Eu$_5$In$_2$Sb$_6$ was found to be much larger than that of the alkaline earth containing A_5In$_2$Sb$_6$ phases (A = Sr, Ca) consistent with the reduced hole effective mass (1.1 m_e). Zn doping was successful in optimizing the carrier concentration, leading to a zT of up to 0.4 at ~ 660 K, which is comparable to that of Zn-doped Sr$_5$In$_2$Sb$_6$.

Introduction

Thermoelectric devices are a viable means to convert waste heat to electrical energy [1]. Efficiency of the overall devices can be improved by using high efficiency materials, which is correlated to the unitless thermoelectric figure of merit, zT, defined by: $zT = \alpha^2 T/\rho\kappa$ [2]. Here α is the Seebeck coefficient, T is temperature, ρ is resistivity, and κ is total thermal conductivity, which has electronic (κ_e), bipolar (κ_B), and lattice (κ_L) components. Engineering efficient thermoelectric materials is challenging because the properties encompassed by zT are interdependent. Thus, in order to achieve high efficiency, a balance must be obtained to ensure a high α and low ρ and κ.

Zintl phases are valence precise compounds comprised of covalently bonded polyanionic structures in combination with cations that provide overall charge balance [3-5]. The structural complexity of many Zintl compounds leads to near-zero optical phonon mode velocity, while their covalently-bonded polyanionic structures contribute to band gap formation and, in some cases, reasonable electronic mobility [5, 6]. Subsequently, Zintl compounds often exhibit low thermal conductivity and tunable electronic properties, making this class of material viable for use in thermoelectric devices [7]. High zT has been achieved in many doped Zintl antimonides including $Yb_{14}MnSb_{11}$ ($zT \sim 1.4$ at 1200 K), $Yb_{14}MgSb_{11}$ ($zT \sim 1$ at 1075 K), $YbCd_2Sb_2$ ($zT \sim 1.26$ at 700 K), $EuZn_2Sb_2$ ($zT \sim 1.06$ at 650 K), $BaGa_2Sb_2$ ($zT \sim 0.6$ at 800 K), which have already demonstrated high efficiencies [8-11].

A number of $A_5M_2Pn_6$ Zintl compounds (A = Ca, Sr, Ba, Eu, Yb; M = Al, Ga, In; Pn = As, Sb, Bi) have been reported in the literature as promising thermoelectric materials [12-19]. The crystal structure of the Zintl antimonide $Eu_5In_2Sb_6$, shown in Fig. 1, was reported to form the $Ca_5Ga_2As_6$ crystal structure with space group *Pbam* (No. 55) by Park *et al.*[19]. Each In atom is four-fold coordinated by Sb atoms to form $InSb_4$ tetrahedra, which are corner-linked along the *c* axis (Fig. 1b). The chains of $InSb_4$ tetrahedra are further bridged by Sb-Sb bonds leading to infinite 1D ladder-like moieties. The Eu atoms between the chains provide electrons to the covalently-bonded anionic framework, yielding an overall charge balance described by: $[A^{2+}]_5[(4b)M^-]_2 [(2b)Pn^-]_4[(1b)Pn^{2-}]_2$. Park *et al.* also reported the low-temperature resistivity and Seebeck coefficients of $Eu_5In_2Sb_6$, which showed semiconducting behavior [19]. Furthermore, they observed decreased resistivity and Seebeck coefficients in a Zn-substituted sample, making $Eu_5In_2Sb_6$ an interesting candidate for further study [14, 15]. In this paper we explore the high temperature electronic and thermal transport properties of $Eu_5In_{2-x}Zn_xSb_6$ ($x = 0$, 0.025, 0.05, 0.1, and 0.2) as well as the room temperature optical absorbance. Additionally, we compare isostructural $A_5In_2Sb_6$ materials to study the bulk effects of the cation site.
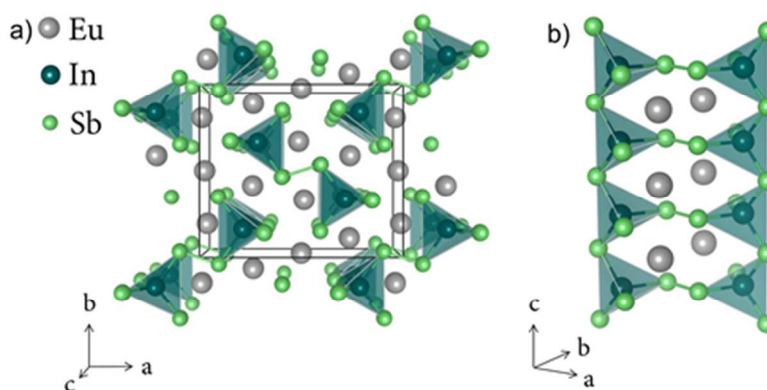
Figure 1: The crystal structure of $Eu_5In_2Sb_6$ contains 26 atoms per unit cell. a) In (blue) and Sb (green) form covalent bonds while Eu (gray) atoms provide overall charge balance. b) Ladder-like chains formed by corner-linked $InSb_4$ tetrahedra along the *c* direction.

Experimental Methods

$Eu_5In_{2-x}Zn_xSb_6$ (x = 0, 0.025, 0.05, 0.1, 0.2) samples were synthesized using the following procedure: In shot (99.999%, Alfa Aesar) and Sb shot (99.9999%, Alfa Aesar) were double vacuum sealed in quartz ampules and heated to 900 K in 6 hours and annealed there for 12 hours then allowed to cool to room temperature in 6 hours to form an InSb precursor. Surface oxide was removed from dendritic Eu (99.9%, HEFA Rare Earth), which was then cut into 1-3 mm pieces in an argon rich glove box and weighed in stoichiometric amounts along with InSb, Sb and Zn foil (99.99%, Alfa Aesar). The elements were then placed inside stainless steel vials with two half inch stainless steel balls and milled using a high energy SPEX Sample Prep 8000 Series Mixer/Mill for 60 minutes. The resulting powder was hot pressed in a POCO graphite die with a 12.7 mm inner diameter sleeve under argon at 823 K and 80 MPa for 2 hours.

Chemical characterization was conducted using X-ray diffraction (XRD), scanning electron microscopy (SEM), energy dispersive X-ray spectroscopy (EDS), and wavelength dispersive X-ray spectroscopy (WDS). An XRD Philips PANalytical XPERT MPD diffractometer with Cu-K_a radiation in reflection mode was used to determine sample purity. A Zeiss 1550 VP was used to conduct SEM and EDS analysis. The chemical compositions of the target phases were determined by WDS using a JEOL JXA-8200 system. The Archimedes method was employed for density measurements. The electrical resistivity, ρ, and Hall coefficient were measured via Van der Pauw technique in a four-point probe setup with tungsten electrodes in a reversible 1 T magnetic field [20]. A two-point Seebeck system using W-Nb thermocouples and light-pipe heating with the temperature gradient across the samples oscillated between ±10 K was used to measure α [21]. Diffuse reflectance infrared Fourier transform spectroscopy (DRIFTS) was carried out with a Thermo Scientific Nicolet 6700 FTIR spectrophotometer equipped with a Harrick Praying Mantis Diffuse Reflection accessory, DTGS detector and KBr beamsplitter [22]. The Kubelka Munk formula: $F(R) = (1 - R)^2/2R$ was used to estimate the scaled absorption coefficient from the raw reflectance data [23]. The free carrier absorption was fit and subtracted using a power law $(FC = a(\hbar\omega)^b + c)$. The absorption edge transition energy was simply estimated as the linear extrapolation of the absorption edge. Thermal conductivity was calculated using $\kappa = dC_pD$, where d is the measured density of material, C_p is estimated from the Dulong-Petit approximation for heat capacity, and D is the thermal diffusivity measured under argon using the laser flash method via a Netzch LFA 457 instrument. The single parabolic band (SPB) model derived from the Boltzmann transport equation within a constant relaxation time approximation (see ref [24] for full equations) was used to approximate an effective mass, m^*, and L [25] assuming acoustic phonon scatting as the main scattering mechanism.

Results and Discussion

Chemical and Structural Characterization: As described in Park *et al.,* $Eu_5In_2Sb_6$ was found to have significant improvement in air stability in comparison to its alkaline earth analogues [19]. All of the samples in this study are > 99% of the theoretical density. The XRD patterns illustrated in Fig. 2 show $Eu_5In_2Sb_6$ is single phase. As the Zn content increases, additional peaks

corresponding to ZnSb become present and increase in intensity. This behavior is reflected in the comparison of the theoretical and experimental carrier concentrations discussed below in Fig. 4, which shows lower than expected carriers for $x \geq 0.1$. SEM and EDS analysis also confirmed the presence of a small amount of Zn-rich secondary phases. The average WDS compositions of target phases, listed in Table 1, indicate successful substitution of In with Zn.

The lattice parameters of all samples were found to be unaltered within standard deviations (Table 1) and are very close to the ones reported by Park *et al.* ($a = 12.510(3)$ Å, $b = 14.584$ (3) Å, $c = 4.6243$ (9) Å) [19]. In the crystal structure, there are $3 \times$ Eu (Eu1 and Eu3: $4g$ ($x, y, 0$); Eu2: $2a$ (0,0,0)), $1 \times$ In ($4h$ ($x, y, \frac{1}{2}$)) and $3 \times$ Sb (Sb1: $4g$ (x, y, 0); Sb2 and Sb3: $4h$ (x, y, $\frac{1}{2}$)) Wyckoff sites. Based on the Rietveld analysis of $Eu_5In_2Sb_6$ (Fig. 3), almost all reflections were indexed with the orthorhombic space group *Pbam* (No: 55). During the refinement, all of the Eu, In, and Sb positions were found to be fully occupied.
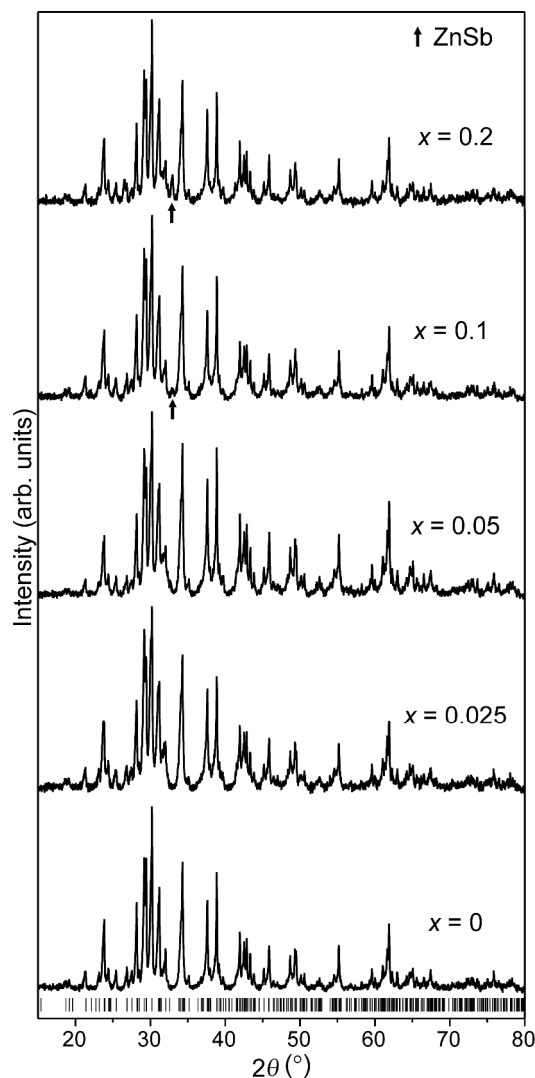
Figure 2: XRD patterns of $Eu_5In_{2-x}Zn_xSb_6$ (Cu-K_{a1} radiation). Calculated peak positions of $Eu_5In_2Sb_6$ are indicated by ticks at the bottom [19]. An increasing amount of ZnSb was observed for samples $x \geq 0.1$—the most intense peaks are indicated by the arrows.

Table 1: WDS compositions show successful substitution of In with Zn. The lattice parameters were nearly unchanged.

Nominal Comp.	WDS Compositions	Lattice Parameters (Å)
$Eu_5In_2Sb_6$	$Eu_{5.13(2)}In_{1.993(7)}Sb_{5.87(2)}$	$a = 12.512(1)$, $b = 14.583(2)$, $c = 4.6296(6)$
$Eu_5In_{1.975}Zn_{0.025}Sb_6$	$Eu_{5.16(2)}In_{1.956(7)}Zn_{0.022(6)}Sb_{5.86(2)}$	$a = 12.514(2)$, $b = 14.583(2)$, $c = 4.6295(5)$
$Eu_5In_{1.95}Zn_{0.05}Sb_6$	$Eu_{5.18(2)}In_{1.926(7)}Zn_{0.049(6)}Sb_{5.85(2)}$	$a = 12.512(2)$, $b = 14.577(2)$, $c = 4.6289(8)$
$Eu_5In_{1.9}Zn_{0.1}Sb_6$	$Eu_{5.13(2)}In_{1.876(7)}Zn_{0.077(7)}Sb_{5.92(2)}$	$a = 12.511(2)$, $b = 14.579(3)$, $c = 4.6274(6)$
$Eu_5In_{1.8}Zn_{0.2}Sb_6$	$Eu_{5.16(2)}In_{1.829(7)}Zn_{0.127(7)}Sb_{5.88(2)}$	$a = 12.517(2)$, $b = 14.584(2)$, $c = 4.6275(8)$
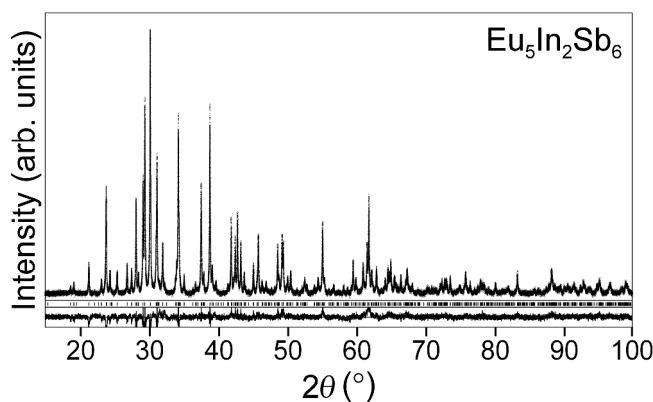
Figure 3: XRD pattern of $Eu_5In_2Sb_6$ (Cu-K_{a1} radiation). Ticks mark the calculated reflection positions of the target phase while the baseline corresponds to the residuals of a Rietveld refinement based on the reported crystal structure ($R_i = 0.07$, $R_p = 0.18$, $R_{wp} = 0.15$) [19].

Electronic Transport Properties: Figure 4 illustrates the increase of the *p*-type Hall carrier concentration, n_H, from $\sim 10^{18}$ h$^+$/cm^3 to $\sim 10^{20}$ h$^+$/cm^3 with increasing Zn content (as determined from WDS), demonstrating that Zn acts as a dopant in the structure. However, the deviation of the experimental values from the predicted trend makes it clear that Zn is not fully soluble for the $x = 0.1$ and 0.2 samples, although both continue to experience a slight increases in n_H. XRD, WDS and carrier concentration data (see Fig. 5) are all consistent with Zn going into the structure and being an effective dopant up to 1 at.% within the investigated composition range. The solubility of Zn in the $Eu_5In_2Sb_6$ structure thus appears to be between that of $Ca_5In_2Sb_6$ and $Sr_5In_2Sb_6$ [14, 15].
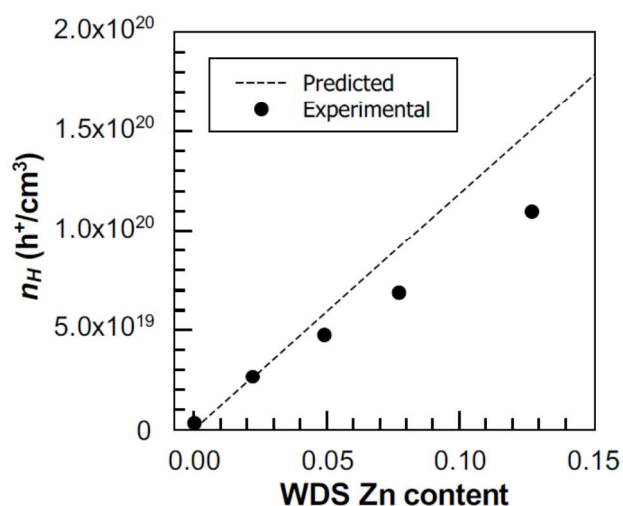
Figure 4: A comparison of the predicted and experimental Hall carrier concentration suggests that the efficiency of Zn doping decreases after a nominal composition of $x = 0.05$.

Figure 5 shows the temperature dependent electronic transport properties for $Eu_5In_{2-x}Zn_xSb_6$ ($x = 0$, 0.025, 0.05, 0.1, 0.2), which illustrates the transition from a non-degenerate semiconductor to a more metallic, extrinsically-doped semiconductor with increasing Zn content. For the undoped sample, n_H increases with temperature as a result of thermally activated charge carriers. The lightly doped $x = 0.025$ phase displays near constant n_H at lower temperatures, but exhibits intrinsic behavior after 500 K, which is reflected in the decreasing ρ and α. The remaining samples display high, nearly temperature-independent carrier concentrations consistent with extrinsically-doped semiconducting behavior.

The resistivity of the undoped sample is consistent with non-degenerate semiconducting behavior. An Arrhenius plot generated from the $\rho \propto e^{E_g/2k_BT}$ relation was used to estimate a band gap of $E_g \sim 0.29$ eV (see inset in Fig. 5c). The addition of Zn decreases the resistivity, consistent with the increases in n_H. The Hall mobility, μ_H, in the undoped sample at 300 K is five times greater than that of $Sr_5In_2Sb_6$ and three times as large as $Ca_5In_2Sb_6$, likely due to the smaller effective mass discussed below (see Fig. 5b) [26]. At low temperatures, μ_H is proportional to e^{-E_A/k_BT}, where E_A is the activation energy, suggesting that μ_H is a heat activated process—possibly the result of impurity oxides or other secondary phases at the grain boundaries [27]. At higher temperatures, μ_H is proportional to $T^{-\nu}$ ($1.0 \leq \nu \leq 1.5$) suggesting that acoustic phonon scattering becomes the main scattering mode [28]. The temperature activated behavior of μ_H explains the negative slope of ρ at lower temperatures seen in the Zn-doped samples, which otherwise display degenerate semiconducting behavior.

The Seebeck coefficients, shown in Fig. 6, are indicative of semiconducting behavior in all samples. Minority carrier activation causes a peak in α at ~ 400 K for the parent compound and $\sim 500 - 600$ K for the doped samples. This early onset of minority carrier activation is consistent

with a small band gap. The Goldsmid-Sharp estimation for the band gap, $E_g = 2e\alpha_{max}T_{max}$, yields $E_g \sim 0.2$ eV, which is lower than the band gap calculated from ρ. A possible explanation for the discrepancy between the two different estimates might be due to n-type minority carriers having higher mobility compared with the p-type majority carriers. This would shift α_{max} and T_{max} to lower values, since high mobility minority carriers contribute disproportionately (and detrimentally) to the Seebeck coefficient [29].

Compared with the report of Park *et al.*, the resistivity and Seebeck coefficients of the undoped sample in this study are significantly greater ($\sim$ 90 compared with $\sim$ 30 mΩ·cm and $\sim$ 160 compared with $\sim$ 80 μV/K, respectively) [19]. This suggests that samples from Park *et al.* had higher carrier concentrations, perhaps due to different synthetic approaches, which can lead to differing concentrations of site defects (Eu deficiency, for example) or impurity phases.

The inset in Fig. 6 illustrates the decreasing Seebeck coefficients with increasing Zn content. The SPB effective mass, m^*, calculated from the Hall carrier concentration n_H via $n = 4\pi(2m^*_{SPB}k_bT/h^2)^{3/2}F_{1/2}(\eta)$ (k_b is Boltzmann's constant, h is Planck's constant, and $F(\eta)$ is the Fermi integral as a function of the chemical potential) yielded m^* of 1.1 m_e at 350 K and 1.35 m_e at 500 K [30]. In Eu$_5$In$_{2-x}$Zn$_x$Sb$_6$, the average m^* is lower than that of Ca$_5$In$_2$Sb$_6$ ($\sim$ 2 m_e at 300 and 500 K) and Sr$_5$In$_2$Sb$_6$ ($\sim$ 1.3 m_e at 350 K and $\sim$ 2.2 m_e at 500 K) as reflected in the mobility [14, 15]. Figure 7 shows that m^* is slightly increasing as a function of n_H in Zn-doped Eu$_5$In$_2$Sb$_6$, but remains relatively constant for Zn-doped Ca$_5$In$_2$Sb$_6$. An increasing SPB effective mass can indicate multiple band behavior, which can favorably influence the Seebeck [31, 32].
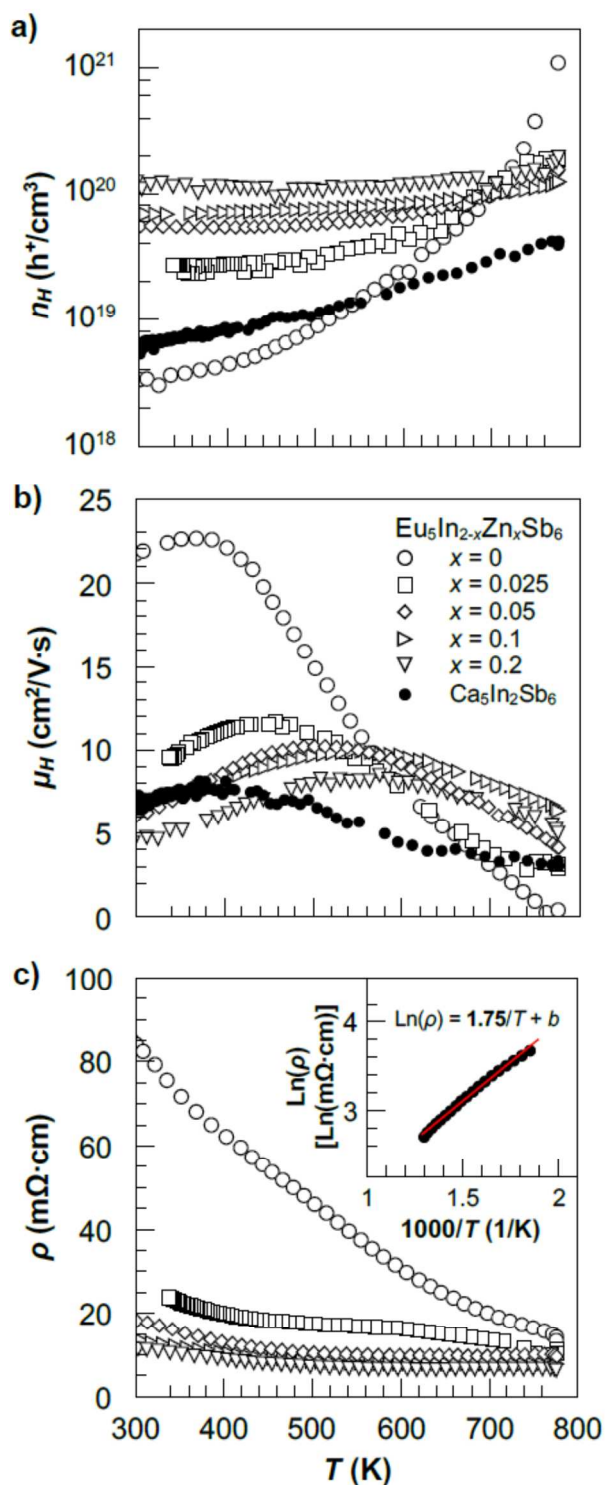
**Figure 5: a)** The addition of Zn increases n_H, suggesting that Zn is acting as a dopant in $Eu_5In_2Sb_6$. **b)** μ_H in the undoped sample is higher than in other $A_5In_2Sb_6$ compounds, and appears to be controlled by an activated process below 500 K. **c)** ρ decreases with increasing dopant concentration. **Inset)** $\rho \propto e^{E_g/2k_BT}$ yields a band gap of $E_g \sim 0.29$ eV.
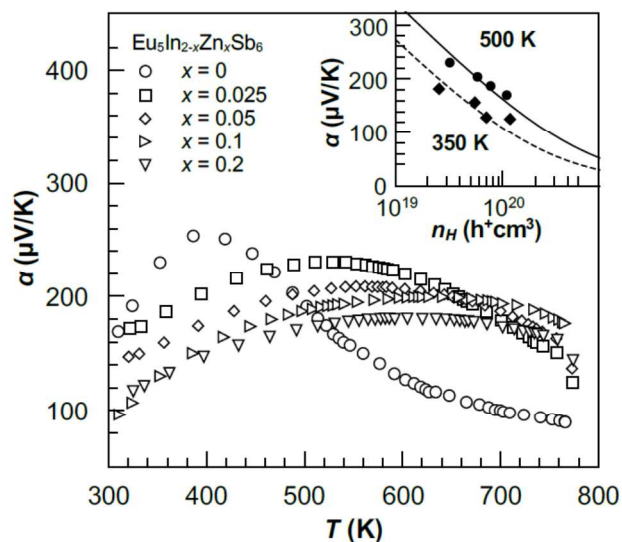
Figure 6: α decreases with increased n_H. A small band gap results in minority carrier activation at lower temperatures. m^* of $1.1\ m_e$ at 350 K and $1.35\ m_e$ at 500 K were used to generate the Pisarenko curves in the inset.
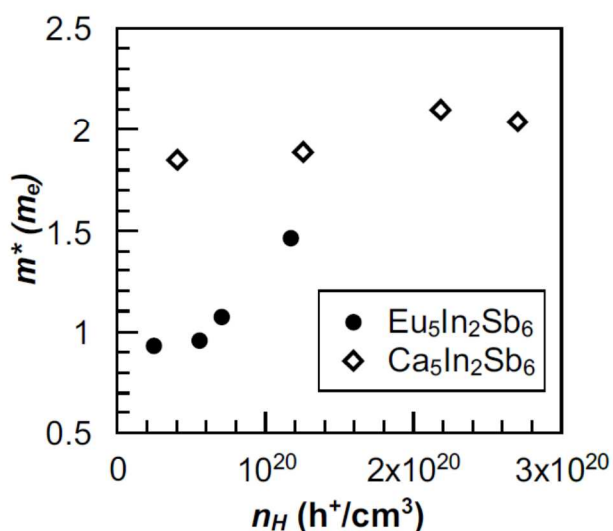
Figure 7: The constant m^* of $Ca_5In_2Sb_6$ suggests single band behavior while the increasing m^* in $Eu_5In_2Sb_6$ hints at two band behavior.

Optical Absorption: Band gaps are estimated using the absorption spectra (minus the free carrier absorption) as shown in Fig. 8. The absorption edge shows two distinct slopes, which likely indicate two transitions, as observed previously for $Sr_5In_2Sb_6$ [15]. The extrapolated gaps for transition one and transition two are 0.15 and 0.27 eV respectively. The presence of two transitions with an energy separation of only ~ 0.1 eV suggests that two band behavior may play an important role in the thermoelectric transport for $Eu_5In_2Sb_6$ [33]. In $Ca_5In_2Sb_6$ and $Sr_5In_2Sb_6$, two transitions were also observed, but a larger band offset suggested that the chemical potential

to overcome the band offset was too large to allow multi band behavior [15]. Furthermore, the carrier dependent effective mass in $Ca_5In_2Sb_6$ seems to be relatively constant—especially at 500 K, indicating good single band behavior [14]. In $Eu_5In_2Sb_6$, on the other hand, the effective mass appears to be steadily increasing—potentially indicating two band behavior (see Fig. 7). As for $Sr_5In_2Sb_6$, more data points are required to confirm a trend [15].
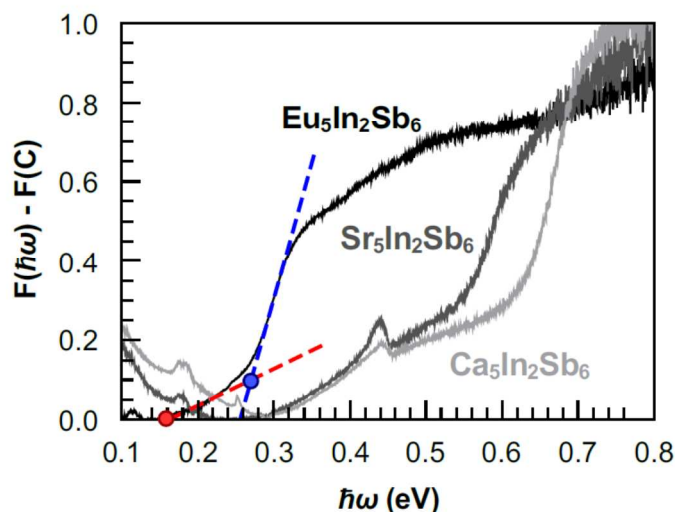
Figure 8: Absorption edge data obtained using DRIFTS for $A_5In_2Sb_6$ (A = Eu, Sr, Ca). The red dashed line is the extrapolation to zero which indicates the first transition and the blue indicates the second transition in $Eu_5In_2Sb_6$. The extrapolated gap values are indicated by the corresponding large dots. $Sr_5In_2Sb_6$ and $Ca_5In_2Sb_6$ have larger transition energies than $Eu_5In_2Sb_6$.

Thermal Transport: The total thermal conductivity, κ (symbols), along with the calculated contribution from $\kappa_L + \kappa_B$ (curves) are shown in Fig. 9. The Lorenz factor, L, used to calculate κ_e from the Wiedemann-Franz law ($\kappa_e = LT/\rho$) is shown in the Fig. 9 inset [7]. The addition of Zn results in slight increases in κ, due mainly to higher κ_e. All samples exhibit low κ_L ($\sim$ 1.1 W/mK at 300 K), which is characteristic of complex Zintl phase materials [6]. At high temperatures, the samples display large κ_B, which is consistent with the system's significant minority carrier contributions. The red dashed line in Fig. 9 indicates the estimated minimum lattice thermal conductivity (at high temperature), $\kappa_{min} \sim$ 0.38 W/mK, calculated from $\kappa_{min} = \frac{1}{2}\left(\frac{\pi}{6}\right)^{1/3} k_B V^{-2/3}(2v_T + v_L)$, where V is the average volume per atom and v_T and v_L are the experimental transverse and longitudinal sound velocities, respectively [34]. Room temperature ultrasonic measurements were used to measure the speed of sound: v_T = 1882 m/s and v_L = 3109 m/s, which are lower in $Eu_5In_2Sb_6$ than in the Ca (v_T = 2115 m/s, v_L = 3710 m/s) and Sr (v_T = 1994 m/s, v_L = 3268 m/s) analogues [26]. Although $Eu_5In_2Sb_6$ has reduced v_T and v_L, at room temperature κ is comparable in all of the $A_5In_2Sb_6$ phases, possibly the result of impurity driven scattering. The experimental high temperature $\kappa_L + \kappa_B$ is observed to be much greater than the κ_{min} due to the large bipolar contribution.
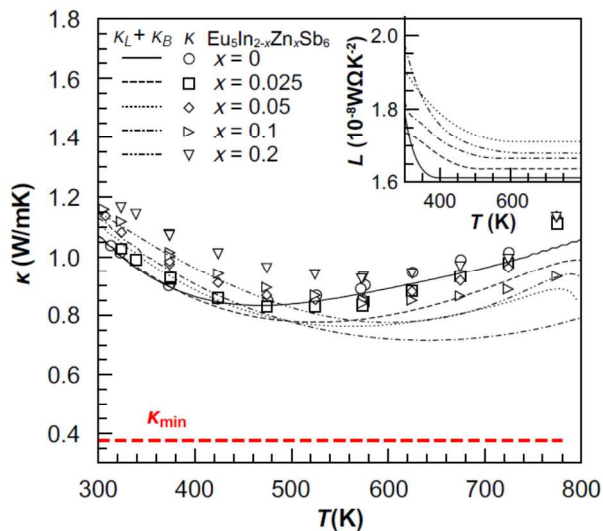
Figure 9: The thermal conductivity of the samples increases as more Zn is added. $\kappa_L + \kappa_B$ are the dominant components in $\kappa - \kappa_B$ has particularly large contributions at higher temperatures. κ_{min} is indicated by the red dashed line. The Lorenz factors used to calculate κ_e are shown in the inset.

Figure of Merit:

The calculated zT curves are shown in Fig. 10. The zT for the undoped sample is below 0.1. However, the zT values increase with increasing Zn content to a maximum of ~ 0.4 at 660 K for $x = 0.1$. This is comparable to Ca and Sr analogues at relative temperatures despite the higher mobility in $Eu_5In_2Sb_5$. The smaller band gap in $Eu_5In_2Sb_5$ leads to minority carrier activation at lower temperatures, ultimately limiting the maximum achievable zT. The predicted zT values estimated using an SPB model are shown as a function of n in the Fig. 10 inset. The following parameters were used to generate the curves at 350 K and 500 K respectively: m^*, of $1.1\ m_e$ and $1.35\ m_e$, intrinsic mobilities, μ_o, of 11 and 13 cm^2/V·s, and κ_L of 1.0 and 0.7 W/m·K. The experimental data is relatively consistent with this simple model, despite possible two band behavior. The deviations from SPB at 500 K for $x = 0.025$ is explained by the presence of minority carriers in that sample. The model suggests that the $Eu_5In_{1.9}Zn_{0.1}Sb_6$ sample has optimized n and zT, which is consistent with the experimental data.
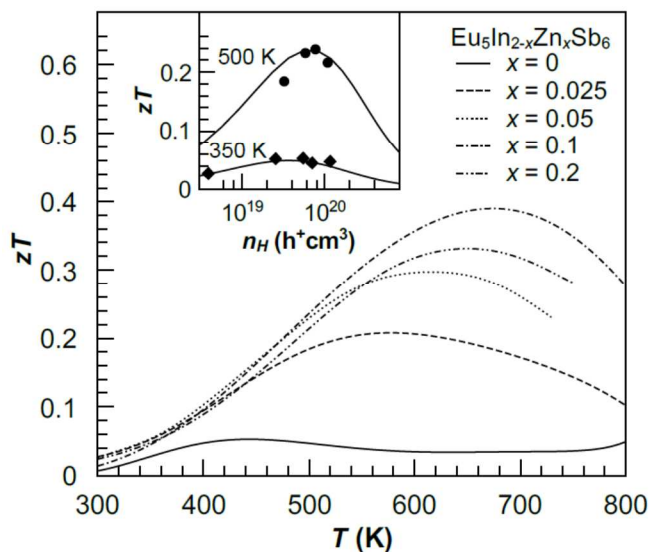
Figure 10: zT plots of $Eu_5In_{2-x}Zn_xSb_6$ ($x = 0$, 0.025, 0.05, 0.1, 0.2). Inset: the SPB generated curves are in good agreement with the experimental zT values for all samples at 350 K and for $x \geq 0.05$ at 500 K.

Conclusion:

$Eu_5In_2Sb_6$ was shown to have significantly improved air stability and electronic mobility relative to other $A_5In_2Sb_6$ (A = Ca, Sr) compounds. $Eu_5In_2Sb_6$ displays non-degenerate p-type semiconducting behavior while the doped samples exhibit degenerate behavior. The efficiency of Zn substituting In decreases after $x = 0.05$, which is comparable to the $Ca_5In_2Sb_6$ case. Band gap approximations from the resistivity and Seebeck data revealed a band gap in the range of 0.2 -0.3 eV. Steadily increasing m^* and the presence of two transitions (one at 0.15 eV and another at 0.27 eV) in the optical absorption spectra might be indicative of two band behavior. However, the small band gap in $Eu_5In_2Sb_6$ relative to $A_5In_2Sb_6$ results in earlier onset of minority carrier activation. Despite the lower longitudinal and transverse sound velocities observed in $Eu_5In_2Sb_6$, the room temperature thermal conductivity is comparable to that $Ca_5In_2Sb_6$ and $Sr_5In_2Sb_6$. Alloying with Ca or Sr may yield lower thermal conductivities and a larger band gap to improve the overall zT of this material.

Acknowledgments

References

1. DiSalvo, F.J., *Thermoelectric Cooling and Power Generation.* Science, 1999. **285**(5428): p. 703-706.
2. Tritt, T.M., *Thermoelectric Phenomena, Materials, and Applications.* Annual Review of Materials Research, Vol 41, 2011. **41**: p. 433-448.
3. Schäfer, H., B. Eisenmann, and W. Müller, *Zintl Phases: Transitions between Metallic and Ionic Bonding.* Angewandte Chemie International Edition in English, 1973. **12**(9): p. 694-712.
4. Kauzlarich, S.M., ed. *Chemistry, Structure, and Bonding of Zintl Phases and Ions*. 1996, VCH Publishers Inc.: New York.
5. A. Papoian, G. and R. Hoffmann, *Hypervalent Bonding in One, Two, and Three Dimensions: Extending the Zintl–Klemm Concept to Nonclassical Electron-Rich Networks.* Angewandte Chemie International Edition, 2000. **39**(14): p. 2408-2448.
6. Kauzlarich, S.M., S.R. Brown, and G. Jeffrey Snyder, *Zintl phases for thermoelectric devices.* Dalton Transactions, 2007(21): p. 2099-2107.
7. Toberer, E.S., A.F. May, and G.J. Snyder, *Zintl Chemistry for Designing High Efficiency Thermoelectric Materials.* Chemistry of Materials, 2010. **22**(3): p. 624-634.
8. Brown, S.R., et al., *Yb14MnSb11: New High Efficiency Thermoelectric Material for Power Generation.* Chemistry of Materials, 2006. **18**(7): p. 1873-1877.
9. Guo, K., Q. Cao, and J. Zhao, *Zintl phase compounds AM2Sb2 (A=Ca, Sr, Ba, Eu, Yb; M=Zn, Cd) and their substitution variants: a class of potential thermoelectric materials.* Journal of Rare Earths, 2013. **31**(11): p. 1029-1038.
10. Aydemir, U., et al., *Thermoelectric Enhancement in BaGa2Sb2 by Zn Doping.* Chemistry of Materials, 2015. **27**(5): p. 1622-1630.
11. Hu, Y.F., et al., *Yb(14)MgSb(11)andCa(14)MgSb(11)-New Mg-Containing Zintl Compounds and Their Structures, Bonding, and Thermoelectric Properties.* Chemistry of Materials, 2015. **27**(1): p. 343-351.
12. Toberer, E.S., et al., *The Zintl Compound Ca5Al2Sb6 for Low-Cost Thermoelectric Power Generation.* Advanced Functional Materials, 2010. **20**(24): p. 4375-4380.
13. Zevalkink, A., et al., *Influence of the Triel Elements (M = Al, Ga, In) on the Transport Properties of Ca5M2Sb6 Zintl Compounds.* Chemistry of Materials, 2012. **24**(11): p. 2091-2098.
14. Zevalkink, A., J. Swallow, and G.J. Snyder, *Thermoelectric properties of Zn-doped Ca5In2Sb6.* Dalton Trans., 2013. **42**: p. 9713-9719.
15. Chanakian, S., et al., *Enhanced thermoelectric properties of Sr5In2Sb6via Zn-doping.* Journal of Materials Chemistry A, 2015. **3**(19): p. 10289-10295.
16. Aydemir, U., et al., *Thermoelectric properties of the Zintl phases Yb5M2Sb6 (M = Al, Ga, In).* Dalton Transactions, 2015. **44**(15): p. 6767-6774.
17. Johnson, S.I., A. Zevalkink, and G.J. Snyder, *Improved thermoelectric properties in Zn-doped Ca5Ga2Sb6.* Journal of Materials Chemistry A, 2013. **1**(13): p. 4244-4249.
18. Nagu, M.P., *Synthesis and thermoelectric studies of Zintl phases in the systems of Ba-Al-Sb, Ba-Ga-Sb, and Ba-In-Sb*. 2014, TU Darmstadt.
19. Park, S.-M., et al., *Eu5In2Sb6, Eu5In2-xZnxSb6: rare earth zintl phases with narrow band gaps.* Journal of Materials Chemistry, 2002. **12**(6): p. 1839-1843.
20. Borup, K.A., et al., *Measurement of the electrical resistivity and Hall coefficient at high temperatures.* Review of Scientific Instruments, 2012. **83**(12): p. 123902.
21. Wood, C., D. Zoltan, and G. Stapfer, *Measurement of Seebeck coefficient using a light pulse.* Review of Scientific Instruments, 1985. **56**(5): p. 719-722.

22.   Zachary, M.G., L. Aaron, and G.J. Snyder, *Optical band gap and the Burstein–Moss effect in iodine doped PbTe using diffuse reflectance infrared Fourier transform spectroscopy.* New Journal of Physics, 2013. **15**(7): p. 075020.

23.   Kubelka, P. and F. Munk, *Reflection characteristics of paints.* Z. Technische Physik, 1932. **12**: p. 593-601.

24.   Zevalkink, A., et al., *Ca3AlSb3: an inexpensive, non-toxic thermoelectric material for waste heat recovery.* Energy & Environmental Science, 2011. **4**(2): p. 510.

25.   Kim, H.-S., et al., *Characterization of Lorenz number with Seebeck coefficient measurement.* APL Materials, 2015. **3**(4): p. 041506.

26.   Zevalkink, A., et al., *Thermoelectric properties and electronic structure of the Zintl phase Sr5In2Sb6 and solid solution Ca5-xSrxIn2Sb6.* Journal of Physics: Condensed Matter, 2015. **27**(1): p. 015801.

27.   Zevalkink, A., et al., *Thermoelectric properties of Sr3GaSb3 – a chain-forming Zintl compound.* Energy Environ. Sci., 2012. **5**: p. 9121-9128.

28.   Amith, A., I. Kudman, and E.F. Steigmeier, *Electron and Phonon Scattering in GaAs at High Temperatures.* Physical Review, 1965. **138**(4A): p. A1270-A1276.

29.   Gibbs, Z.M., et al., *Band gap estimation from temperature dependent Seebeck measurement—Deviations from the 2e|S|maxTmax relation.* Applied Physics Letters, 2015. **106**(2): p. 022112.

30.   Ohno, S., et al., *Thermoelectric properties of the Yb9Mn4.2–xZnxSb9 solid solutions.* Journal of Materials Chemistry A, 2014. **2**(20): p. 7478.

31.   Crocker, A. and L. Rogers, *VALENCE BAND STRUCTURE OF PbTe.* Journal de Physique Colloques, 1968. **29**(C4): p. C4-129-C4-132.

32.   Zhou, M., et al., *Optimization of thermoelectric efficiency in SnTe: the case for the light band.* Physical Chemistry Chemical Physics, 2014. **16**(38): p. 20741-20748.

33.   Gibbs, Z.M., et al., *Temperature dependent band gap in PbX (X = S, Se, Te).* Applied Physics Letters, 2013. **103**(26): p. 262109.

34.   Toberer, E.S., A. Zevalkink, and G.J. Snyder, *Phonon engineering through crystal chemistry.* Journal of Materials Chemistry, 2011. **21**(40): p. 15843.

High Temperature Thermoelectric Properties of Zn-doped Eu$_5$In$_2$Sb$_6$

Sevan Chanakian[1], Umut Aydemir[1*], Alex Zevalkink[1,2], Zachary M. Gibbs[3], Jean-Pierre Fleurial[2], Sabah Bux[2], G. Jeffrey Snyder[1]

Graphical Abstract Entry

The Zintl phase Eu$_5$In$_{2-x}$Zn$_x$Sb$_6$ (x = 0, 0.025, 0.05, 0.1, 0.2) with optimized p-type carrier concentration displays a zT of up to 0.4 at ~ 660 K.

Graphical Abstract